Materials Characterization 235 (2026) 116260

Contents lists available at ScienceDirect

Materials Characterization

journal homepage: www.elsevier.com/locate/matchar

Dissimilar gas tungsten arc welding of an AlCoCrFeNi high entropy alloy to 316 L stainless steel

J.G. Lopes [a,*], P. Agrawal [b,c], R.M. Gonçalves [d], J. Shen [a], D. Chassaing [e], T. Boll [e], N. Schell [f], R.S. Mishra [b,c], A.C. Baptista [a], J.P. Oliveira [a,*]

[a] CENIMAT/I3N, Department of Materials Science, NOVA School of Science and Technology, Universidade NOVA de Lisboa, 2829-516 Caparica, Portugal
[b] Center for Friction Stir Processing, Department of Materials Science and Engineering, University of North Texas, Denton, TX 76207, USA
[c] Advanced Materials and Manufacturing Processes Institute, University of North Texas, Denton, TX 76207, USA
[d] UNIDEMI, Department of Mechanical and Industrial Engineering, NOVA School of Science and Technology, Universidade NOVA de Lisboa, Caparica 2829-516, Portugal
[e] Karlsruhe Nano Micro Facility (KNMF), Institute of Applied Materials (IAM-WK), and Institute for Nanotechnology (INT), Karlsruhe Institute of Technology (KIT), Hermann-von-Helmholtz-Platz 1, 76344 Eggenstein-Leopoldshafen, Germany
[f] Institute of Materials Physics, Helmholtz-Zentrum Hereon, Max-Planck-Str. 1, 21502 Geesthacht, Germany

ARTICLE INFO

Keywords:
High entropy alloys
Gas tungsten arc welding
Synchrotron X-ray diffraction
Atom probe tomography
Microstructure
Mechanical testing
Thermodynamic simulations

ABSTRACT

High entropy alloys (HEAs) are unique and novel materials with remarkable properties that render them competitive for developing key engineering applications within modern engineering sectors. In the present study, a AlCoCrFeNi HEA was gas tungsten arc welded to 316 L stainless steel, with the aim of assessing the compatibility in terms of microstructure and mechanical performance. These dissimilar joints was obtained with a torch speed of 3.5 mm/s and a current intensity of 90 A under a protective Argon atmosphere. Subsequently, a thorough evaluation of the relationship between processing parameters, microstructure and properties was performed via optical and electron microscopy, atom probe tomography, synchrotron X-ray diffraction, microhardness mapping and tensile testing. The results reveal that the AlCoCrFeNi HEA can be successfully welded with 316 L stainless steel, producing a high-quality and reliable joint, where a gradual microstructural variation is observed across the interface. A good balance of a high tensile strength of ≈568 MPa and fracture strain of ≈11.7% was obtained, with fracture occurring in the fusion zone, highlighting the potential of these dissimilar joints for critical structural applications.

1. Introduction

An increasing trend for studying novel and advanced materials contemporaneously known as high entropy alloys (HEAs), has been noticeable throughout recent years [1,2]. Such a trend represents the intent for the pursuit of new materials conveyed by modern-day scientists for updating and strengthening the conceptual requirements behind modern day engineering applications. Such, from the author's point of view, is facilitated by the fact that HEAs present themselves with the possibility of tailoring their properties with a specific requirement in target, given the wide compositional space available for their development. For this reason, HEAs are unique and novel materials with remarkable properties that render them competitive for developing key engineering applications within modern engineering sectors.

To further exploit this compositional flexibility, the design of HEAs can be guided through integrated computational and experimental approaches. Thermodynamic modeling methods such as CalPhaD (Calculation of Phase Diagrams) enable the prediction of phase stability and equilibrium relationships across complex multicomponent systems, thereby assisting in the identification of promising alloy compositions [3]. In parallel, machine learning techniques have increasingly been employed to uncover composition–structure–property relationships and accelerate the exploration of the vast HEA compositional space [4]. These computational strategies are commonly followed by experimental investigations focusing on alloy processing and microstructural characterization, allowing the influence of processing routes on phase formation and resulting properties to be assessed [5,6]. Through this combined approach, HEAs can be systematically tailored and optimized

* Corresponding authors.
E-mail addresses: jcg.lopes@fct.unl.pt (J.G. Lopes), jp.oliveira@fct.unl.pt (J.P. Oliveira).

https://doi.org/10.1016/j.matchar.2026.116260
Received 23 December 2025; Received in revised form 5 March 2026; Accepted 10 March 2026
Available online 15 March 2026

to meet the specific demands of targeted engineering applications.

Moreover, out of the many HEA compositions researched since their inception in 2004 [7,8], dual-phase HEAs are excellent candidates for structural applications. Within this sector, honorable mentions are the $Fe_{50}Mn_{30}Co_{10}Cr_{10}$ [9] and the CoCuFeMnNi [10] HEA systems, however, one that stands out is the AlCoCrFeNi HEA. This HEA system presents itself with a dual-phase nature composed mainly of a disordered FCC phase and an ordered B2 BCC phase. Several studies have already highlighted its outstanding performance in diverse environments, where Parakh et al. [11] highlighted the correlation between phase fraction and corrosion resistance, while Tian *et al.* [12] studied its hot deformation behavior under a wide range of working conditions.

However, before jumping to conclusions concerning the wide possibilities for their usage in the industry, research on their processability must be addressed to avoid any unnecessary predicaments that may hinder finalized products. One of the most prominent processes within the industrial world is fusion-based welding, namely gas tungsten arc welding (GTAW). GTAW offers the ability to permanently merge single parts into complex shaped components and induces profound microstructural changes in them due to the high temperatures required for localized fusion. On this topic, the literature already showcases an effort to comprehend the effects that GTAW has on the AlCoCrFeNi HEA system [13,14], allowing us to take on the next step which is to evaluate its metallurgical compatibility with other materials via dissimilar welding.

On this topic, the literature showcases several studies where dissimilar welding of HEAs was successfully accomplished mainly in the CoCrFeMnNi HEA via GTAW [15–19] and laser [20,21] welding technologies. However, of special interest is the research conducted by Sokkalingam et al. [22] in 2019, on GTAW of a $Al_{0.1}$CoCrFeNi to AISI 304 steel, where the suitability of the obtained joint was noted to be suitable for structural applications, exhibiting a significantly higher tensile strength (corresponding to ≈590 MPa) than the analyzed HEA. Moreover, dissimilar weldability of the AlCoCrFeNi system to 316 L stainless steel (316 L SS) was conducted by Li et al. [23] and Zhu et al. [24] via spot welding and electron beam welding, highlighting the feasibility of achieving defect-free fusion with graded microstructures on these two systems. In this sense, a recent study by Ma et al. [25] showcased the possibility for joining an as-rolled eutectic AlCoCrFeNi HEA to SS 316 L via GTAW, evaluating microstructure and mechanical performance. Their results showed that the fusion zone (FZ) exhibited a mixed microstructure comprising both columnar and equiaxed grains, with the grain phases predominantly consisting of an FCC structure. At the same time, the dissimilar welded joint achieved a tensile strength of 1042 MPa and an elongation of approximately 22%. Vickers hardness measurements across the welded joint revealed significant variation among the FZ, heat-affected zone (HAZ), and base metal (BM), with the highest hardness observed on the $AlCoCrFeNi_{2.1}$ side near the fusion boundary.

Although substantial, such results can be strengthened via continuous analysis of AlCoCrFeNi HEA system with other materials. As such, in this paper, we delve into the study of dissimilar welding of a nearly eutectic AlCoCrFeNi HEA with 316 L stainless steel (316 L SS), adding to the current state of the literature an analysis conducted via conventional and advanced analysis techniques. These include namely optical and electron microscopy, high energy synchrotron X-ray diffraction (SXRD), atom probe tomography (APT) and mechanical testing, at both nano, micro and macroscales. Additional details on the solidification paths undertaken by the molten pool are further analyzed via CalPhaD to understand the microstructure obtained in the welded joint. Therefore, the study aims to he novelty of this study lies in providing a sturdy analysis of the compatibility between a nearly eutectic AlCoCrFeNi HEA and 316 L stainless steel that can achieved via GTAW.

2. Materials and methods

In this work, 30 × 30 mm plates (with a thickness of 1.5 mm) of an as-cast AlCoCrFeNi HEA system were welded with a commercially available 316 L SS (see composition in Table 1) using the in-house developed GTAW apparatus showcased in Fig. 1, which was connect to a CITOTIG 2200 FORCE welding equipment.

The welding parameters comprised a torch speed of 3.5 mm/s, a constant electrode-to-sample distance of 1.5 mm, and a current intensity of 90 A. Commercially pure Argon (99.999% purity) was applied as shielding gas with a flow of 16 and 6 L/min on the face and root of the weld, respectively. Prior to welding, both materials were cleaned with acetone and parameter optimization tests were carried out. Initial trials were performed on each BM separately to identify a stable processing window, which was then used as the basis for the subsequent optimization for obtaining the dissimilar joints.

To assess the microstructure changes induced by the weld thermal cycle, conventional metallographic preparation methods were used, where the cross-section of the joint was cut via electric discharge machining and subsequently polished following a standard metallographic procedure. For electron backscatter diffraction (EBSD) analysis, the samples were ground progressively with sandpapers of increasing grit size, followed by polishing with diamond paste. A final polishing step was performed using colloidal silica to achieve a smooth and deformation-free surface. No chemical etching was applied prior to EBSD testing, ensuring that the microstructure was preserved for accurate diffraction pattern acquisition. Following this, scanning electron microscopy (SEM) imaging, energy dispersive X-ray spectroscopy (EDS) and EBSD were performed using a FEI Nova NanoSEM 230 equipped with EDAX Hikari Super EBSD detector. The samples were then etched with aqua regia (composed of 1 part of nitric acid to 3 parts of hydrochloric acid, respectively), which enabled to perform optical microscopy using a Leica DMI5000 M inverted microscope.

Synchrotron X-ray diffraction was performed at the P07B beamline at Petra III in DESY, Germany, to determine the existing phases across the different regions of the joints. The setup involved working in transmission mode setup, with an incoming X-ray beam with a wavelength of 0.14235 Å. The joint was probed using a beam size of 250 × 500 μm for 0.7 s, with a 250 μm spacing between each scan. Scanning was performed from one side of the base material going through the fusion zone (FZ) and finishing on the opposite BM. For further advanced nanoscale characterization, a LEAP™ 4000× HR (Cameca Instruments) equipped with a reflection lens was used for APT, where samples were retrieved from regions of interest within the FZ using a focused ion beam (FIB). The analyses were conducted at a temperature of 50 K with a laser pulse energy of 50 pJ and was operated in laser pulsing mode at a pulse repetition rate of 125 kHz. Data analysis was performed using the software IVAS 3.8.4.

To understand the influence that the mixture between the AlCoCrFeNi HEA and 316 L SS will have on the microstructure upon their mixing and subsequent solidification, CalPhaD-based calculations were conducted using Thermo-Calc software, aided by the TCHEA 5.1 database. Such was achieved via the Scheil-Gulliver module, which aids in the simulation of phases that are prone to nucleate during the fast cooling and non-equilibrium solidification of the molten pool (which is characteristic of arc-based processes).

For mechanical properties assessment, microhardness maps of the weld were conducted using a Mitutoyo Micro Hardness Testing Machine HM-112, with a load of 0.5 kg and dwell time of 10 s. Moreover, tensile specimens were cut by Electrical Discharge Machining (EDM) and subsequently subjected to light surface grinding to remove micro-fissures associated with the cutting process. No dimensional modification or cross-section homogenization was performed, ensuring the as-fabricated

Table 1
– Composition of SS 316 L (wt%) [26].

Cr	Ni	Mo	Mn	Si	C	Fe
18	12	2	0.75	0.5	0.02	Balance

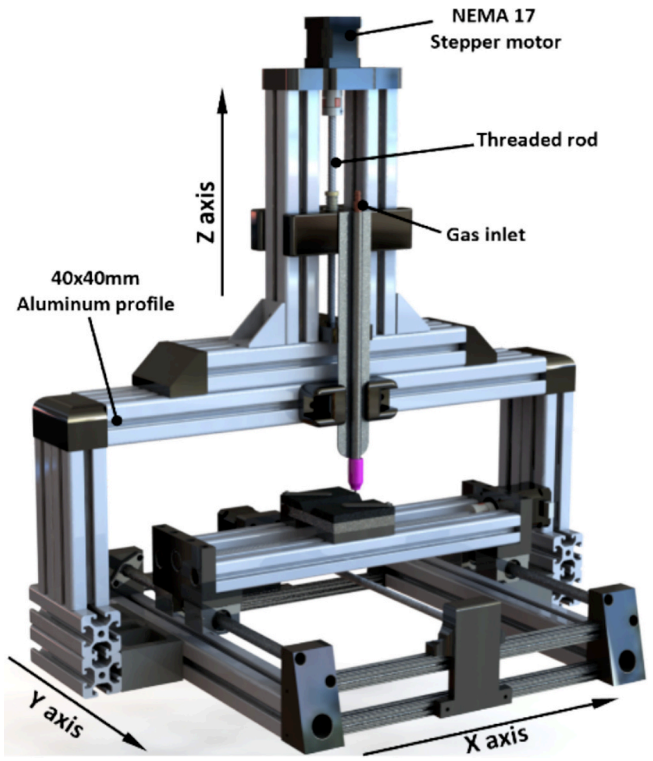

Fig. 1. GTAW experimental apparatus.

geometry was preserved to reflect realistic loading conditions. Tensile testing was performed using an autograph Shimadzu AG50kNG machine at a displacement rate of 1 mm/min, with the tensile force applied perpendicular to the welding direction. Simultaneously, digital image correlation (DIC) data was recorded, and the resulting fracture surfaces were then imaged with an HITACHI SU8000 SEM.

3. Results and discussion

3.1. Microstructural characterization of the welded joint

A representative optical micrograph of the cross-section of the dissimilar joints is shown in Fig. 2 (a). There, the evident distinction of the AlCoCrFeNi BM, the FZ and the 316 L SS BM (from left to right), can easily be identified. Furthermore, as it is known from the well-established microstructure developed during GTAW, a HAZ is expected to develop on both sides of the FZ due to high temperatures attained close to it [27,28]. Such is the case of the 316 L SS side, where an increasing gradient grain size can be observed when going from the BM towards the FZ. Nevertheless, due to the large dendritic nature of the AlCoCrFeNi BM, the HAZ on this side of the joint is not easily noticeable via microscopy techniques.

At this macro level, the compositional differences between both BMs are further highlighted in the EDS maps in Fig. 2 (b), where a clear distinction between the distribution of all the analyzed elements can be observed. As expected, while Al, Co and Ni are more prevalent in the AlCoCrFeNi side of the weld, the amount of Fe is higher in the 316 L SS BM, and with Cr practically evenly dispersed throughout the weld.

Furthermore, the microstructure of the weld is highlighted in Fig. 2 (c), where a collage of consecutive EBSD inverse pole figure (IPF) maps can be observed, representing the whole extension of the welded joint, while allowing to observe the variation in grain orientation along the joint.

With particular emphasis on the FZ, which develops through solidification of the molten pool, a pronounced gradient in grain size and morphology is observed as the interface transitions from one BM to the other. This spatial variation is governed by the interplay between the local temperature gradient (G) and the solidification rate (R), which together determine the stability of the solid–liquid interface during solidification. From a solidification thermodynamics perspective, the ratio G/R controls the extent of constitutional supercooling ahead of the advancing interface. When the temperature gradient is sufficiently high relative to the growth rate, the solidification front remains stable,

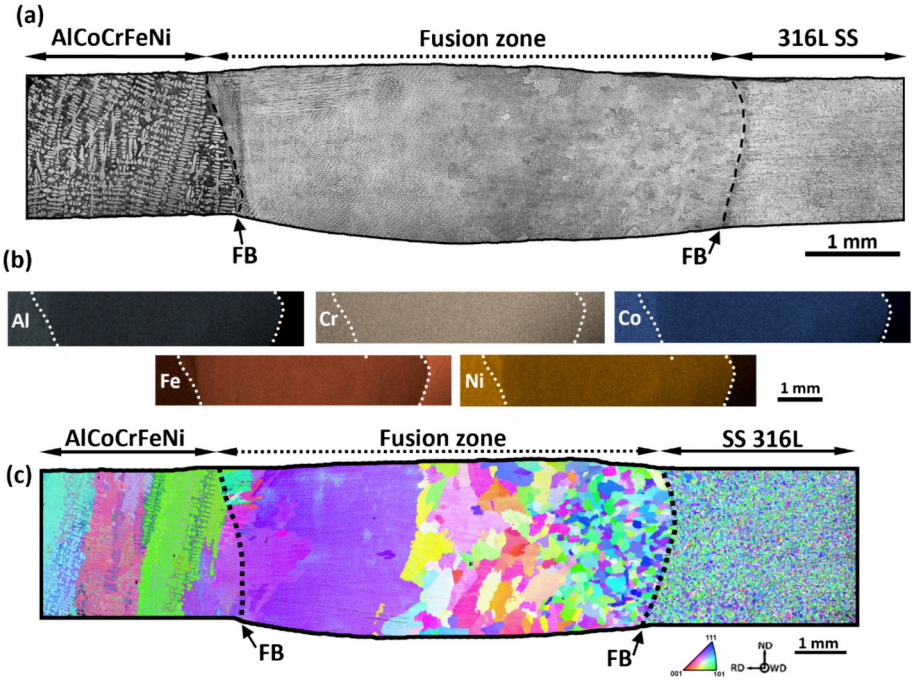

Fig. 2. Optical microscopy of the cross-section of the dissimilar weld: (a) Macrograph highlighting the FZ and the two BMs; and (b) EDS maps displaying an overall perspective of the elemental distribution throughout the joint (c) Collage of IPF EBSD maps of the dissimilar welded joint, highlighting the variation in grain orientation and morphology throughout the joint. (FB corresponds to the fusion boundary).

favoring directional heat extraction and epitaxial growth from the fusion boundary. Under these conditions, columnar dendritic structures preferentially develop and extend along the direction of maximum heat flow [29].

Conversely, when the G/R ratio decreases, the solid–liquid interface becomes increasingly susceptible to constitutional supercooling, which promotes interface instability and facilitates the nucleation of new grains within the molten pool. This transition enhances the formation of finer and more equiaxed grains. Therefore, the progressive variation in thermal gradient and growth rate across the melt pool, together with epitaxial solidification at the fusion boundary and subsequent competitive grain growth, collectively governs the observed microstructural heterogeneity across the FZ.

As evidence of epitaxial growth, which refers to the tendency of the grains to grow with the same crystallographic orientation as those already present in the BM, it can be seen that the region of the FZ closer to the AlCoCrFeNi BM showcases grains with a similar color tone, i.e., possessing similar grain orientation, as the ones that can be found in the HEA near the fusion boundary (FB). The same can be said for the FZ grains closer to the 316 L SS BM, where a tendency to lean towards a bluish color tone, i.e., ⟨111⟩ orientation, can be seen.

On the other hand, competitive growth is noticeable at the central region of the FZ, where the grains that are oriented more favorably in their easy growth direction (which is ⟨001⟩ for cubic structures), which are now far from the influence of each BM, tend to increase in size at the expense of other grains present within this region. However, before the microstructural changes occurring during GTAW can be closely inspected, it is necessary to infer the microstructural condition of each BM. For this, representative EBSD maps taken from both BMs are displayed in Fig. 3.

Starting with the AlCoCrFeNi HEA BM (refer to Fig. 2 (a)), the microstructure is mainly composed of large FCC grains, averaging 83.6 ± 23.5 μm in size, which are surrounded by a eutectic constituent composed of both FCC and B2 BCC phases. Further analysis via EDS allowed us to quantify the composition of the present HEA, which corresponds to 14.9% of Al, 16.5% of Co, 18.1% of Cr, 17.4% of Al and 33.4% of Ni (all values in at. %).

Furthermore, while a comprehensive discussion on a similar HEA's microstructure was conducted in [13], it can be inferred that such large dendritic features are a product of the cooling conditions and elemental segregation that took place during solidification of the original casting block used to obtain this BM. Such is to be expected from the time and temperature factors imposed on the ingot, which was left to cool down slowly during its production [30].

Similar conclusions can be drawn from the analysis of Fig. 4, where we can see that while the FCC phase is mainly composed of Co, Cr, and Fe, the B2 BCC phase is richer in the Al and Ni, further highlighting the effects of elemental segregation during solidification.

On the opposite side of the welded joint is the 316 L SS BM. A representative EBSD map of this region is depicted in Fig. 2 (b). There we can see that the 316 L SS BM is composed of small equiaxed grains with an approximate size of 19.8 ± 2.3 μm. Within the grains, it is also possible to observe several twins, which have their inception associated with growth accidents in the stacking sequence within the grain structure during recrystallization and grain growth phenomena arising from the high temperatures achieved during the hot rolling process [31].

With a fundamental basis established regarding the initial state of each BM, it is now possible to evaluate the microstructural evolution that is visible when progressing *towards* the bulk of the FZ and is a direct product of the GTAW process. As such, Fig. 5 delves into the analysis of the two FBs which are located at the interface of the FZ with each HAZ side. There, once again, the HAZ in the AlCoCrFeNi HEA side cannot easily be distinguished. Nevertheless, beyond this fact, a sharp microstructural transition between each FB can be observed directly through the different grain sizes and morphology that developed with the proximity to each BM, as it going to be discussed next.

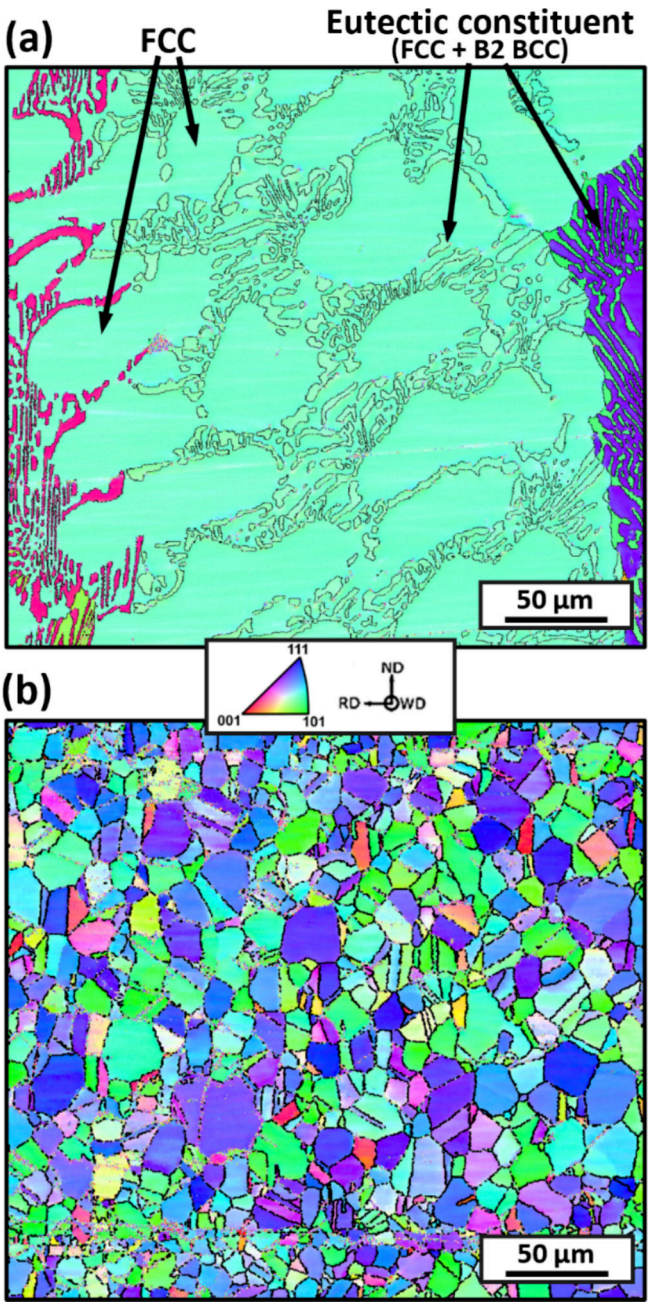

Fig. 3. Representative EBSD maps of the BMs: (a) AlCoCrFeNi HEA and (b) 316 L SS.

A close-up view of each FB reveals large grains composed of smaller dendritic structures within the FZ can be seen in Fig. 5 (c) and (d), contrasting with the structures present in each HAZ. Such differences are caused by the different temperature conditions experienced by each region of the weld, where the HAZ tends to experience recrystallization and grain growth phenomena, while the FZ undertakes complete remelting and subsequent solidification.

Furthermore, it is also possible to locate a partially melted zone (PMZ) between the HAZ and the FZ on the 316 L SS side of the joint (see Fig. 5 d)). This region is formed due to the segregation-induced liquation at the FCC matrix grain boundaries of the FCC matrix of the 316 L SS. In such cases, alloying elements/impurities in the grains that decrease the melting temperature of the BM, segregate towards the grain boundaries during its manufacturing. Upon reaching the high temperatures during welding, these lower melting temperature grain boundaries tend to melt,

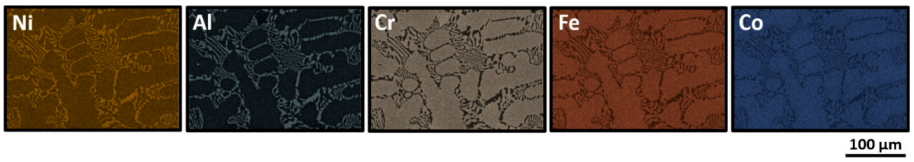

Fig. 4. EDS maps of the AlCoCrFeNi HEA BM.

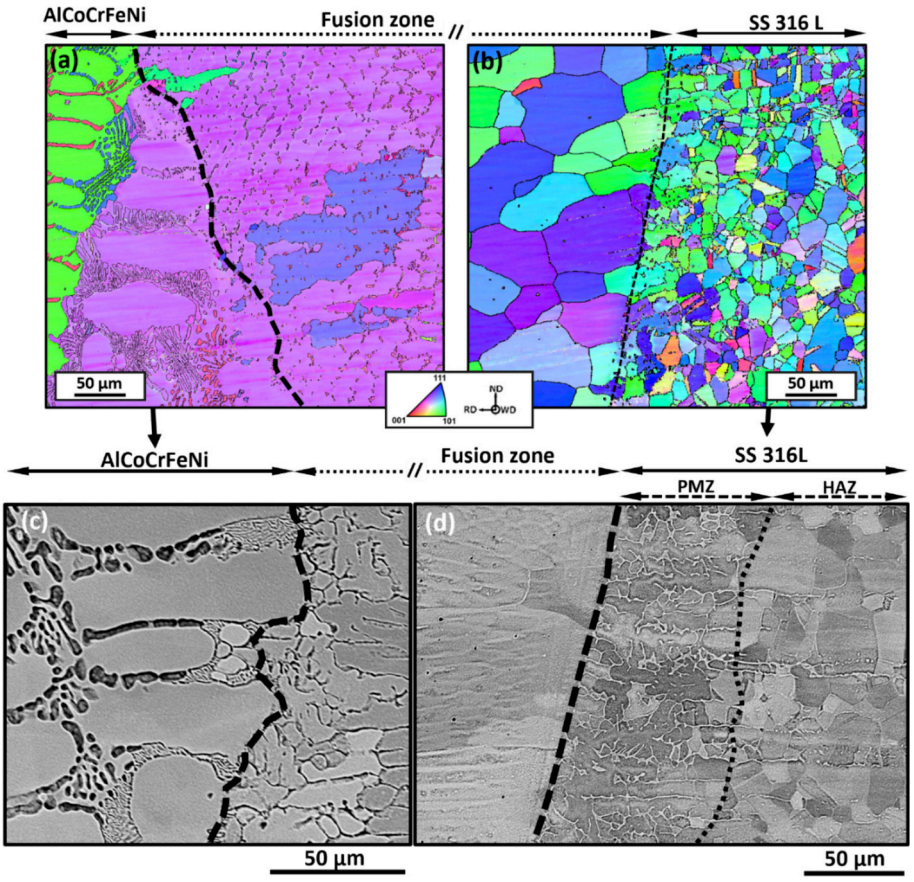

Fig. 5. Microstructural features at the fusion boundary: a) EBSD maps obtained on the AlCoCrFeNi side and b) 316 L SS side. SEM micrographs highlighting the sharp microstructural differences, i.e., grain size and morphology variations, can be observed in c) for the AlCoCrFeNi side and d) for the 316 L SS side of the weld.

leaving the remaining portion of the grains in the solid state [27]. This allows the material in this region to undergo to solid + liquid domain state instead of reaching a full liquid condition.

Aside from that, another interesting fact that can be observed is the discrepancy in grain size on the FZ, at both FBs. In this sense, the grains near the AlCoCrFeNi HEA side are larger than the grains closer to the 316 L SS HAZ. This can be associated with the grain size on each side of the joint, where larger size leads to less nucleation events occurring at the solid/liquid interface. Furthermore, EDS maps taken from the two FBs can be observed in Fig. 6, qualitatively revealing a similar elemental distribution of the FZ to the HEA side of the weld and a sharp compositional change near the FB at the 316 L SS side, especially regarding Al,

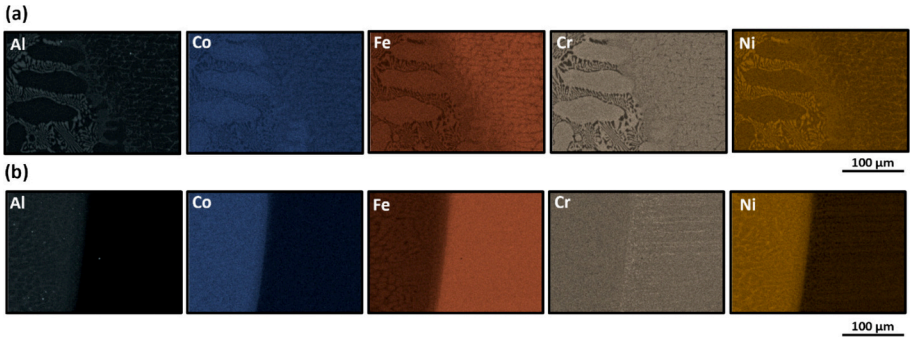

Fig. 6. EDS mapping at the fusion boundary near the: a) AlCoCrFeNi HEA and b) 316 L SS BMs.

Co and Ni.

Further into the FZ and evoking the microstructural gradient evolution visible in Fig. 2 a) and c), we delve deeper into the characteristics mainly in its bulk and at its two extremes (near the AlCoCrFeNi HEA and the 316 L SS sides). These regions of the FZ are exhibited on the EBSD IPF maps of Fig. 7 a), b) and c). There we can observe that both the grain size and the size of the cross-section of the dendrites that compose them are drastically different. That is, by comparison of the two extremes, while the FZ near the AlCoCrFeNi HEA does not have a sufficient amount of visible grains due to their massive size (near 1 mm), the grains closer to the 316 L SS BM have an approximate size of 69.6 ± 20.0 μm. In the middle of the FZ, grains tend to have a size of 210.2 ± 85.9 μm. As mentioned, this showcases the impact that proximity to each BM had during solidification, in terms of, composition and thermal conductivity, affecting the cooling rate and the thermal gradient responsible for final grain size and morphology [27].

From these two peripheral regions, APT tips were produced to investigate small compositional fluctuations that occur due to the

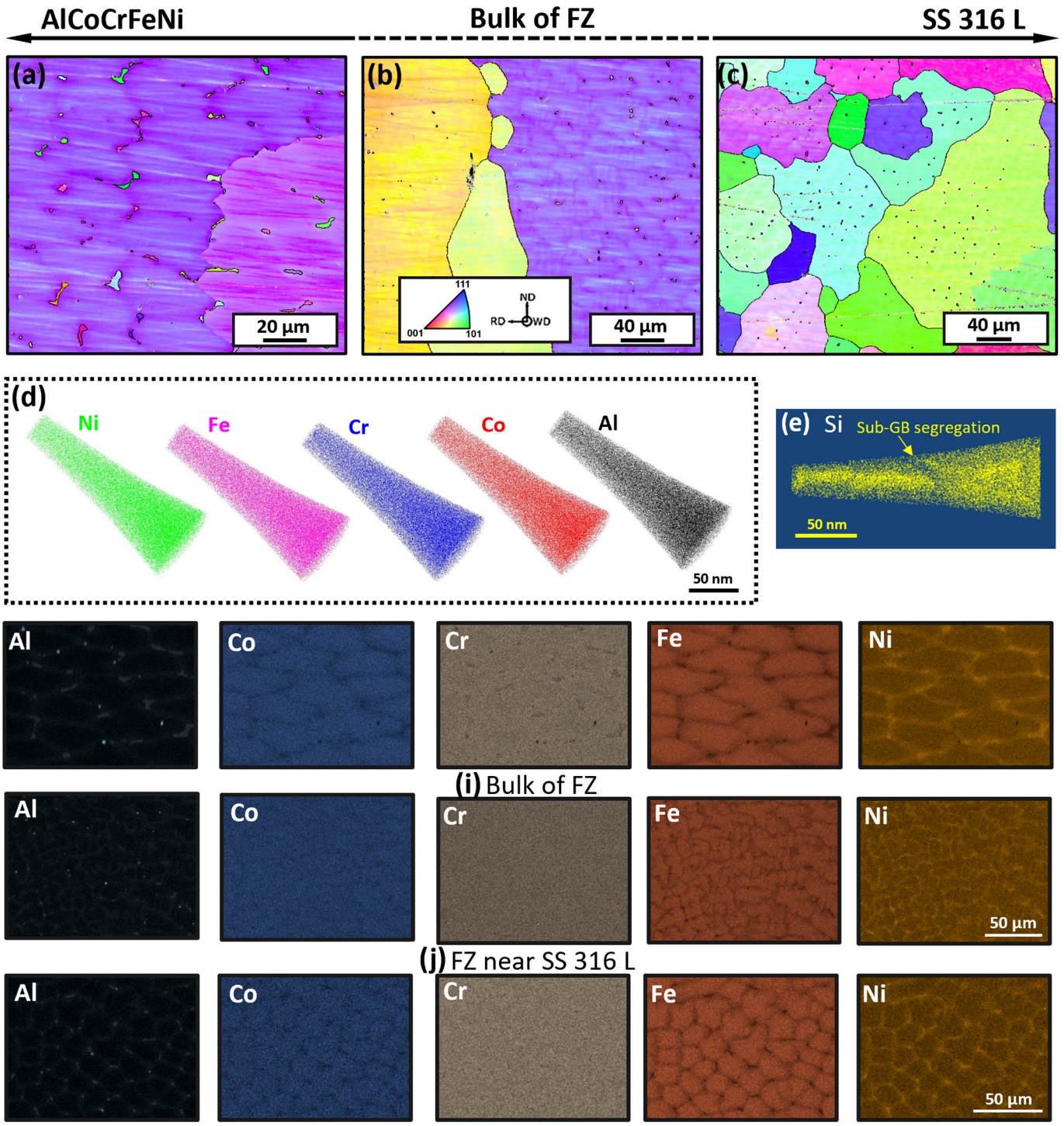

Fig. 7. EBSD maps obtained (a) near the AlCoCrFeNi HEA, (b) at the bulk and (c) near the 316 L SS side of the FZ, alongside (d) representing the composition at obtained at each of these regions utilizing APT ad (e) highlighting segregation of Si near the 316 L SS side. The EDS maps in (f), (g) and (h) highlight the composition of each examined regions.

elemental segregation or due to the presence of nano-sized precipitates within the FZ. The observations are depicted in Fig. 7 d) and reveal that through the FZ, the analyzed region indicate an homogeneous distribution of all elements, at a nano level. Nevertheless, observing the obtained compositional results in Fig. 7 e), which was obtained in the FZ region near the 316 L SS BM, it can be seen that segregation of Si occurred at the sub-grain boundaries (sub-GB), that is at the dendritic level.

Apart from that, considering a broader compositional analysis, Fig. 7 f), g) and h) displays EDS maps corresponding to the three investigated regions of the FZ. For these, aside from the evident disparity in grain size, it is also possible to observe that, in terms of location within the grains, the elemental distribution is identical. This means that, in both cases, Al and Ni tend to segregate towards the grain boundaries during solidification of the molten pool, while Co, Cr and Fe are present in more quantity within the dendritic cores. A similar elemental distribution can be observed in the AlCoCrFeNi HEA, which presents a dendritic microstructure in its BM (see Fig. 4). The quantitative results obtained from Fig. 7 are shown in Table 2.

3.2. Synchrotron X-ray diffraction analysis

To further assess the welded joint microstructure beyond the features that can be noticed through surface inspection methods (optical and electron microscopy) high energy synchrotron X-ray diffraction scans were taken from the joint. These scans were obtained on both base materials and from two different regions of the FZ, each near both BMs. These results are displayed in Fig. 8. Due to the relatively large grain size and the limited synchrotron beam size (250 × 500 μm), the measurements were used for phase identification to avoid poor statistics and overinterpretation on quantitative phase analysis.

Concerning both base materials, the results indicate that the 316 L SS comprises both an austenitic FCC phase alongside a ferritic BCC phase, as indexed (refer to Fig. 8 (a)). This is in good agreement with the previous analysis performed in [17], where the lower intensity ferrite peaks corresponded to a low phase fraction on the microstructure. On the other side of the weld, regarding the AlCoCrFeNi HEA, the respective diffraction patterns show that this BM is composed mainly of two main phases: a disordered FCC and a B2 (ordered) BCC phase, accompanied by peaks corresponding to nanosized $L1_2$ (ordered FCC) phase particles present within the microstructure, as previously highlighted in [32].

Regarding the HAZ, it still is not possible to easily observe and distinguish this region in the AlCoCrFeNi HEA, while on the 316 L SS side, we can see an increase in the ferrite (BCC) peak intensity, as marked by the red circles in Fig. 8, close to the interface between the BM and the FZ. This indicates the presence of the PMZ in between the HAZ and the FZ on the 316 L SS BM side of the weld.

Considering the FZ, it is possible to observe that the diffraction patterns coming from each analyzed region are distinct from each other, although having in common the presence of a predominant FCC phase, whose composition varies concerning its distance from each BM, as seen previously.

Despite this, both sides of the FZ exhibit peaks corresponding to the FCC, B2 BCC, BCC and the $L1_2$ FCC phases, similar to those found within both BMs and thus suggesting the mixing of both materials during welding. In addition to this, however, the difference between each FZ mainly resides in peak intensity.

Table 2
Compositional measurements in FZ obtained by EDS (at.%).

FZ region	Al	Co	Cr	Fe	Ni
Bulk	8.0	9.6	19.3	40.8	22.3
Near AlCoCrFeNi HEA	8.7	10.1	19.2	38.6	23.4
Near 316 L SS	8.6	10.0	19.2	39.2	23.0

3.3. Thermodynamic analysis of the mixture between the HEA and 316 L SS

Investigating the thermodynamic compatibility between both types of BMs aids in identifying the possible phases that may form during their mixing and subsequent solidification, thus potentially enabling the avoidance of potential detrimental effects caused by undesired precipitates. Following this route, non-equilibrium solidification calculations based on the Scheil-Gulliver method were performed considering the partial mixture of the 316 L SS BM into the AlCoCrFeNi HEA, as shown in Fig. 9 (a). The compositions utilized for this analysis are detailed in Table 3.

There it is possible to observe the temperature at which the material starts to solidify ($T_{liquidus}$), the temperature at which the solidification process terminates ($T_{solidus}$) and the temperature for the formation of a eutectic constituent ($T_{eutectic}$) in terms of the ratios between each BM. In addition to this, the phases that are prone to nucleate within the microstructure are also highlighted. Within the range of 0 to 20% of 316 L SS, where the composition is closer to the HEA system, the microstructure is predicted to be composed of an FCC phase and ordered B2 BCC. In the other extreme, where the compositions are closer to the 316 L SS BM, the microstructure is composed of the disordered FCC and BCC phases. In between, these two extremes, the thermodynamic calculations reveal the nucleation of these three phases, where the ordered B2 BCC phase only nucleates at the final solidification stages (being practically isothermal, as shown in Fig. 9 (b)).

Likewise, it must be mentioned that within the compositional extremes corresponding to each BM, the variation in solidification temperature ($T_{liquidus}$ - $T_{solidus}$) is smaller, while the value of $T_{liquidus}$ is closer to $T_{eutectic}$. Such results on a composition capable of forming the eutectic constituent, albeit highlighting the difference in solidification temperature, which is lower in the HEA case, where the molten material stays liquid for longer (provided the same starting temperature). Beyond this, an overall, increasing trend for $T_{liquidus}$ to increase with the growing percentage of 316 L SS, can also be observed.

Further inspection of the Scheil curve obtained for the FZ (calculated based on the averaged compositions presented in Table 2), allows us to situate the obtained curve between the 50–60% of 316 L SS composition, which is displayed in Fig. 9. There it is possible to observe that the solidification path is composed of two stages, where, in the first instance, the FCC phase starts forming (at 1376 °*C*) until reaching 1320 °*C*, corresponding to the eutectic point, at which the conditions for the disordered BCC phase to nucleate are attained. Eventually, in the final solidification stage, the conditions for the formation of the ordered BCC B2 phase are reached, at 1250 °*C*, where the solidification process finalizes. This agrees with the obtained microstructure where large FCC grains are visible within the FZ.

With the elemental distribution data retrieved from the FZ Scheil-Gulliver curve, the partition coefficient for each of the elements present within the FZ was calculated by dividing the amount of each component of each solid phase by the corresponding amount in the liquid phase. The results are shown in Fig. 9 (c). As such, during solidification, should the partition coefficient decrease, it means that its concentration in the liquid is being segregated from the forming microstructure towards the remaining liquid, and vice-versa. Given this, both phases in the two stages of solidification showcase a similar evolution in terms of the partition coefficient. Furthermore, apart from Ni and Al, all elements tend to increase above the value 1, which corresponds to the point where the concentration of a component within the liquid equals the concentration within the solid. As such, these elements, namely Co, Cr and Fe, contribute to the formation of the FCC matrix, while Ni and Al are segregated towards the interdendritic fluid up to the point where the conditions for the nucleation of the B2 BCC phase are met, thus producing the eutectic constituent. Such results are coherent with the elemental maps displayed in Fig. 7. Nevertheless, it is also important to mention that evidence of a eutectic structure was not found

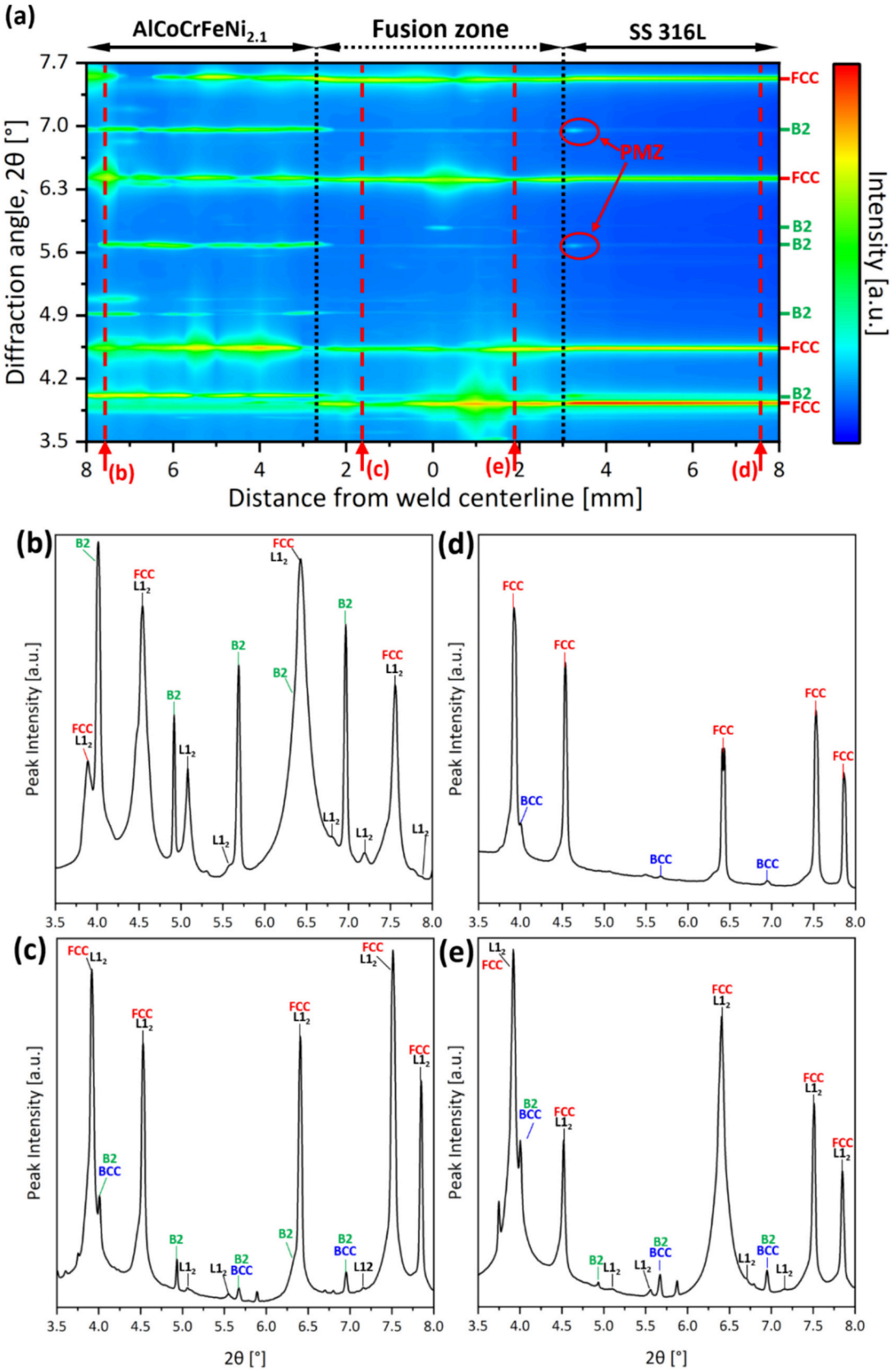

Fig. 8. Synchrotron X-ray diffraction analysis of the welded joint: (a) superimposition of full azimuthal integrated diffraction over the full extent of the joint (major peaks from the FCC and BCC B2 phases are marked on the left side of the map). Representative synchrotron X-ray diffraction scans were obtained from: (b) AlCoCrFeNi HEA BM; (c) 316 L SS BM; (d) FZ near the AlCoCrFeNi HEA and (e) FZ near the 316 L SS BM. Peaks coming from 2nd harmonic reflections, due to P07b/ PETRA III beamline conditions, were left unidentified.

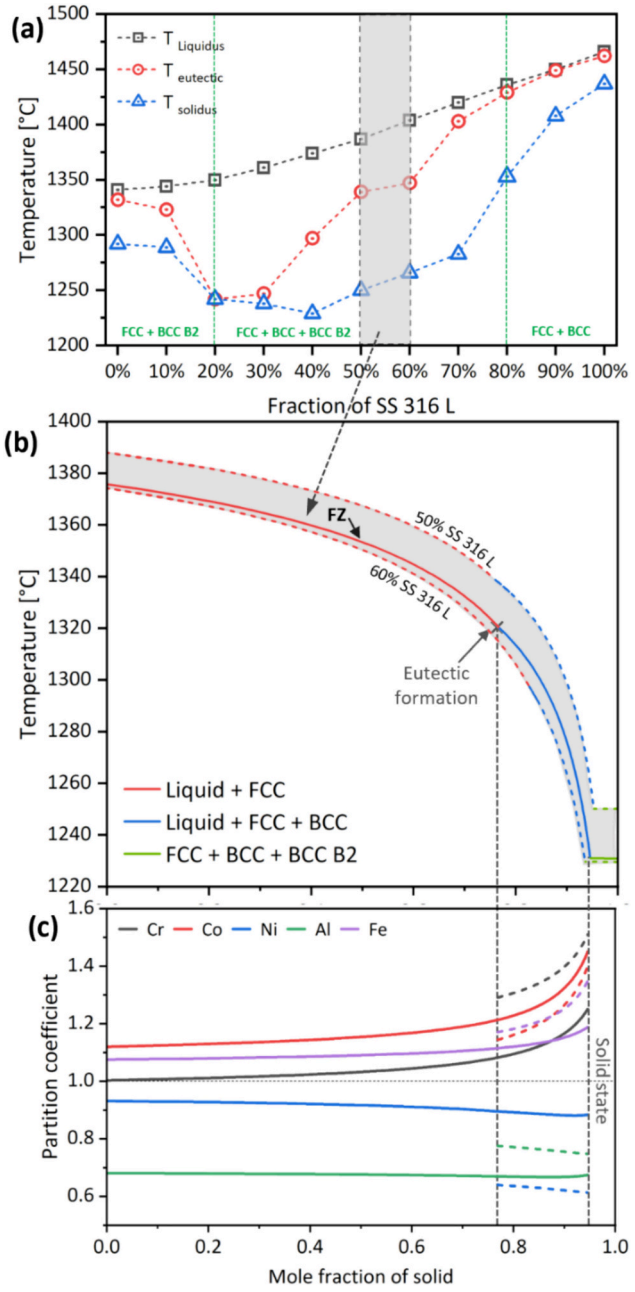

Fig. 9. CalPHaD-based simulation of the phases that may develop during solidification: (a) variation of Liquidus, solidus and eutectic temperatures with an increasing amount of 316 L SS; (b) Scheil-Gulliver solidification curves corresponding to the FZ and the compositions of 50% and 60% of the mixture of 316 L SS; and (c) partition coefficient evolution of the FZ.

by the applied microscopy techniques. Such can be due to the mentioned solidification conditions imposed in the molten pool by the welding process, thus slightly deviating the solidification path from the predicted microstructure. Corroborating this fact is the non-prediction of the $L1_2$ nanoprecipitates, which are possible to be detect via SXRD.

3.4. Microhardness distribution throughout the welded joint

Fig. 10 displays a microhardness map taken from the cross section of the weld, where it is possible to observe the impact of the varying microstructure on the local mechanical behavior per region of the joint.

Starting from the BMs, the AlCoCrFeNi HEA has an average hardness of 221 ± 3 HV_{500g} while the 316 L SS showcases an average of 169 ± 5 HV_{500g}. However, in the HAZ, an increase in hardness can be observed in both cases, with the HAZ on the HEA side reaching 247 ± 10 HV_{500g} and in the 316 L SS side attaining values of 162 ± 12 HV_{500g}. In the HEA side the increase of hardness can be explained by the precipitation strengthening effect of nanosized $L1_2$ and BCC phases on this region as explained by Xiong et al. [33] for the same HEA system.

On the other hand, the hardening observed in the HAZ of the SS 316 L is attributed to the localized alteration of the microstructure, particularly regarding the phase fraction and morphology of BCC phase in detriment of the FCC phase of this BM. This is further influenced by diffusion-driven redistribution of alloying elements and solid solution strengthening at high temperature, which contributes to local variations in lattice distortion and hardness. Such is evident by the fact that diffraction peak intensity is highly related to phase fraction, as well as grain texture, and Fig. 8 indicates an uneven distribution of peak intensity in the HAZ close to the FZ. Given this, variations in phase fraction and grain structure lead to heterogeneity in mechanical properties, resulting in increased hardness compared to its corresponding BM.

Furthermore, observing the FZ we can observe a non-constant variation in hardness, which can be related to the gradient of microstructure and composition that exists throughout the joint. On the HEA side, the joint hardness is 155 ± 4 HV_{500g}, however, when going towards the center of the FZ it increases, reaching 173 ± 9 HV_{500g}. Closer to the 316 L SS side, however the hardness is 153 ± 6 HV_{500g}. These microhardness fluctuations arise from microstructural and compositional gradients within the fusion zone. Regions near the fusion boundaries experience stronger dilution from the adjacent base materials and relatively finer solidification structures, which locally increase hardness. In contrast, the weld center solidifies later and develops comparatively coarser dendritic structures, resulting in the observed variations in microhardness. This behavior aligns with the microstructural features (refer to Fig. 2), as the 316 L SS BM is mainly composed of an FCC matrix, while the AlCoCrFeNi HEA exhibits a composite microstructure of a softer FCC phase and a harder ordered BCC B2 phase, alongside $L1_2$ nanoprecipitates. Nevertheless, the pronounced gradient in grain size governs the local mechanical behavior, with the Hall–Petch relationship remaining the primary controlling factor in the mechanical response of the FZ.

Table 3
Compositions utilized for Scheil-Gulliver calculations (all values in at. %).

Fraction of 316 L SS	Fe	Cr	Co	Ni	Al	Fraction of HEA
100%	73.0	17.4	0.0	9.6	0.0	**0%**
90%	67.4	17.5	1.7	12.0	1.5	**10%**
80%	61.9	17.5	3.3	14.3	3.0	**20%**
70%	56.3	17.6	5.0	16.7	4.5	**30%**
60%	50.8	17.7	6.6	19.0	6.0	**40%**
50%	45.2	17.8	8.3	21.4	7.5	**50%**
40%	39.6	17.8	9.9	23.7	8.9	**60%**
30%	34.1	17.9	11.6	26.1	10.4	**70%**
20%	28.5	18.0	13.2	28.4	11.9	**80%**
10%	23.0	18.0	14.9	30.8	13.4	**90%**
0%	17.4	18.1	16.5	33.1	14.9	**100%**

3.5. Tensile testing coupled with digital image correlation and fractography

Fig. 11 depicts the results obtained by tensile testing the welds in comparison to both base materials, considering only engineering values. The representative stress/strain curves of the welded joint show that the fracture occurred at a strain of ≈12.7%. The maximum tensile stress was achieved at ≈568 MPa, corresponding to a strain of ≈11.4%. The 316 L SS base material, achieved a maximum of 432 MPa (corresponding to a strain of ≈54.6%) eventually fracturing at a strain of ≈56.6. The AlCoCrFeNi HEA, however, achieved the higher value for maximum tensile stress, ≈892 MPa, at a strain of ≈14.4%. From this is possible to

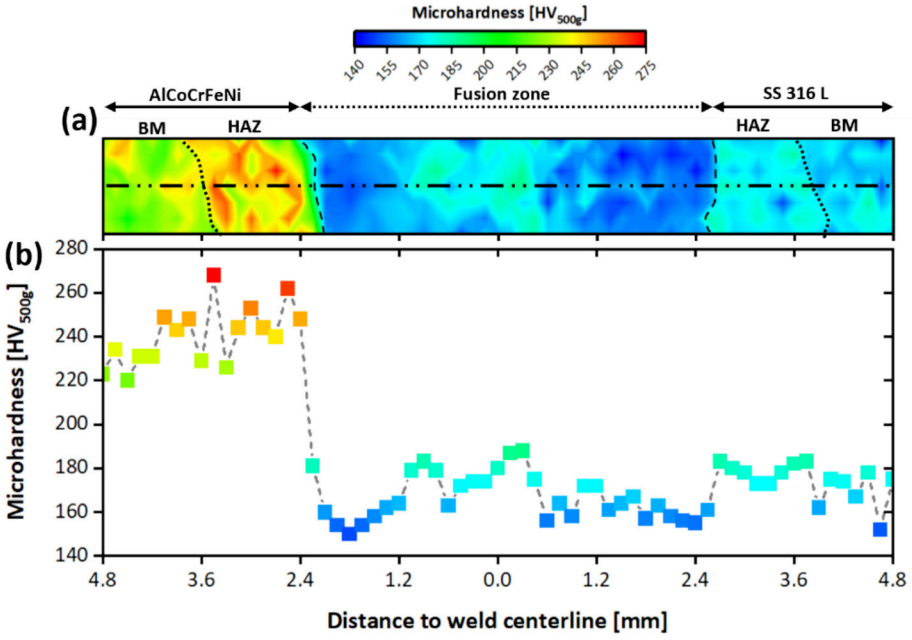

Fig. 10. Microhardness map of the dissimilar welding joint, highlighting the differences arising from the varying microstructure.

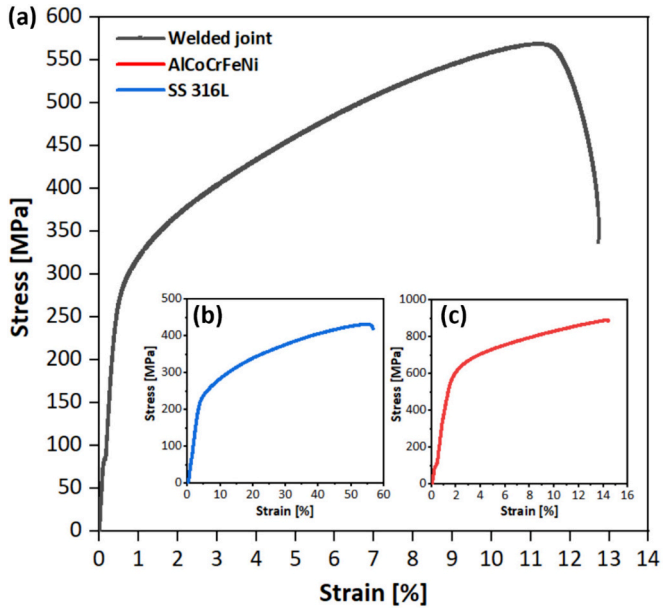

Fig. 11. Representative mechanical response to tensile stress of: (a) the welded joints; (b) 316 L SS base material and (c) AlCoCrFeNi HEA base material.

conclude that the weld reached a similar mechanical response concerning the maximum tensile stress of the 316 L SS BM while maintaining the strain at which it fractured similar to the AlCoCrFeNi HEA BM.

The DIC data, as shown in Fig. 12 (a), exhibits the different mechanical behavior highlighted by each of the different regions of the welded joint, which when spatially averaged considering the full extension of the joint yields the macroscopic mechanical response of weld shown in Fig. 11.

Of special interest, we can observe that the side of the joint that sustained most of the plastic deformation corresponded to the FZ reaching 53% of strain. This can be related to the highly columnar dendritic grain morphology and associated crystallographic texture in this region, limiting uniform dislocation storage and strain-hardening and thus leading to localized deformation and reduced toughness relative to the other regions. This behavior is followed by the 316 L SS BM side, whereas the HEA side of the joint remained practically unaffected, thus highlighting the superior mechanical strength of the HEA. Such can be especially noted in Fig. 12 (b), where further analysis of the behavior of region-specific points allows further elucidation on the local mechanical behavior on the joint. There, beyond the fact that was already noted in terms of BMs, we can see that the HAZ on both sides presents itself with a similar mechanical behavior, with that of the HEA showcasing a 20% higher strain than the 316 L SS side. Such behavior on the HAZ near the HEA, albeit exhibiting higher hardness values, is expected to occur due to the effect of the larger grain size visible in Fig. 2 and Fig. 6.

Furthermore, observing closely the shape of the FZ (marked in purple) in Fig. 11, it is possible to observe a change in slope after a strain of 13% is reached. Such phenomenon occurring upon deformation of the FZ may be linked to elemental dilution that occurs during the formation of the molten pool, thus making it more favorable for the activation of strain accommodation mechanisms other than dislocation slip, such as twining.

Upon eventual failure of the joint, which in the present case occurred in FZ, the fractured surface (refer to Fig. 12 (c)) reveals several dimples characteristic of a ductile-like fracture, which is in line with that expected from the analyzed mechanical performance of the joint.

4. Conclusions

Dissimilar welding between a dual-phase AlCoCrFeNi HEA and commercially available 316 L SS was successfully conducted via GTAW. While the grain size within the FZ showcases a clear transition from one BM to another, it can be observed that a larger size is prominent close to the HEA side of the joint. As such, the following conclusions can be drawn:

- The 316 L SS BM is characterized by an homogenous distribution of the constituent elements, and equiaxial microstructure throughout its full extent. The same is not applicable to the HEA, where a fully dendritic microstructure is composed of large FCC grains with a eutectic constituent in their midst, with the latter being rich in Al and Ni.

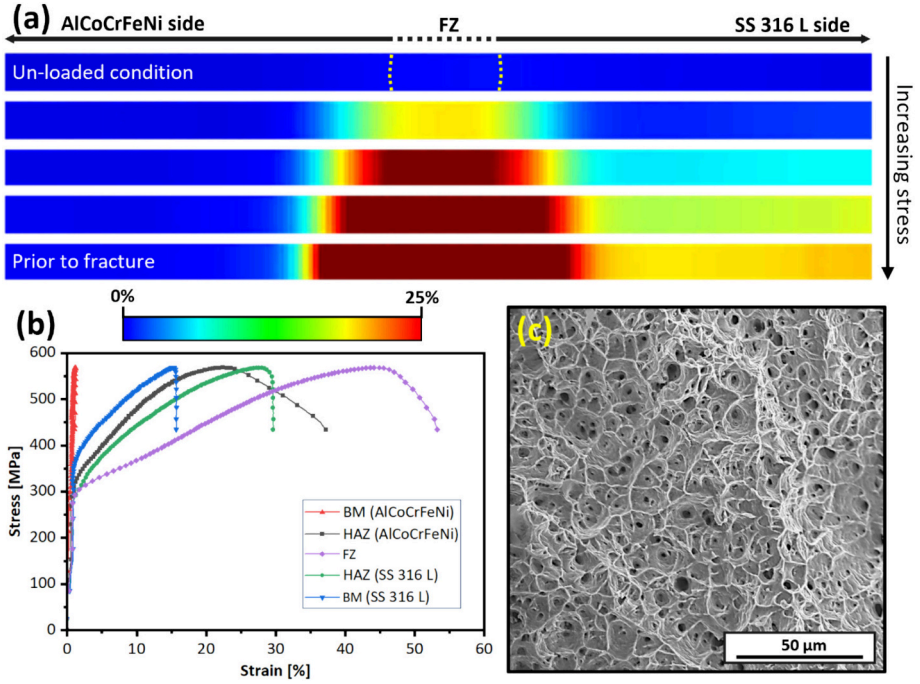

Fig. 12. Digital image correlation results exhibiting: (a) the local strain distribution before fracture, (b) point analysis obtained during tensile testing; and (c) fracture surface after failure of the sample characterized solely by dimples.

- A closer look on the FZ, showcases a similar compositional distribution throughout its full extent, with FCC as its matrix. Further analysis of the FZ via APT, reveals no significant changes within key areas of the FZ, except for the segregation of Si when near the 316 L SS side of the joint.
- Synchrotron X-ray diffraction conducted on the FZ, revealing the presence of an ordered $L1_2$ FCC phase and a disordered BCC phase, beyond those already identified via microscopy, namely FCC and BCC B2. Such results were coherent with the thermodynamic-based calculations, which hinted at the formation of a disordered BCC phase during solidification.
- Mechanical performance analysis highlighted a clear distinction of the regions that comprise the weld can be found within the microhardness maps, with the FZ reaching values close to the 316 L SS BM. This was also verified via tensile testing with the aid of DIC data, where most of the imposed strain is imparted by the 316 L SS BM.
- Overall, the welds attained an excellent strength and ductility balance, with a maximum tensile stress of ≈568 MPa and eventual fracture occurring in the FZ, at a strain of ≈11.7%.

The present data highlights the excellent weldability between the AlCoCrFeNi HEA system and 316 L SS, hinting at the possibility of introducing HEAs in modern day engineering applications.

CRediT authorship contribution statement

J.G. Lopes: Writing – review & editing, Writing – original draft, Visualization, Validation, Project administration, Methodology, Investigation, Formal analysis, Data curation, Conceptualization. **P. Agrawal:** Investigation. **R.M. Gonçalves:** Investigation, Data curation. **J. Shen:** Methodology, Investigation. **D. Chassaing:** Investigation. **T. Boll:** Investigation, Data curation. **N. Schell:** Investigation. **R.S. Mishra:** Investigation. **A.C. Baptista:** Investigation. **J.P. Oliveira:** Writing – review & editing, Visualization, Supervision, Investigation.

Declaration of competing interest

The authors declare that they have no known competing financial interests or personal relationships that could have appeared to influence the work reported in this paper.

Data availability

The data will be shared using Mendeley data:Lopes, J G. (2026), "AlCoCrFeNi HEA and SS316L welded joint - NFFA DATA", Mendeley Data, V1, doi: 10.17632/y2bm6p27ct.1

Acknowledgements

JGL and RMG acknowledge FCT - Fundação para a Ciência e a Tecnologia, I.P. for its financial support via the project UID/00667/2020 (UNIDEMI). JGL, RGM and DM acknowledge FCT - Fundação para a Ciência e a Tecnologia, I.P. for funding the Ph.D. grants 2020.07350.BD, 2022.11133.BD and 2023.154786.BD, respectively. AC, JS, DM and JPO acknowledge the funding by national funds from FCT - Fundação para a Ciência e a Tecnologia, I.P., in the scope of the projects LA/P/0037/2020, UIDP/50025/2020 and UIDB/50025/2020 of the Associate Laboratory Institute of Nanostructures, Nanomodelling and Nanofabrication – i3N. The authors acknowledge DESY (Hamburg, Germany), a member of the Helmholtz Association HGF, for the provision of experimental facilities. Beamtime was allocated for proposal I-20231128 EC. The research leading to this result has been supported by the project CALIPSOplus under the Grant Agreement 730872 from the EU Framework Programme for Research and Innovation HORIZON 2020. This project has received funding from the European Union's Horizon 2020 research and innovation programme under grant agreement No 101007417, having benefited from the access provided by KIT (Germany) within the framework of the NFFA-Europe Pilot Transnational Access Activity, proposal ID161.

References

[1] E.P. George, D. Raabe, R.O. Ritchie, High-entropy alloys, Nat. Rev. Mater. 4 (8 4) (2019) 515–534, https://doi.org/10.1038/s41578-019-0121-4.

[2] Y. Tang, R. Wang, B. Xiao, Z. Zhang, S. Li, J. Qiao, S. Bai, Y. Zhang, P.K. Liaw, A review on the dynamic-mechanical behaviors of high-entropy alloys, Prog. Mater. Sci. 135 (2023) 101090, https://doi.org/10.1016/J.PMATSCI.2023.101090.

[3] W. Wang, Z. Li, M. Han, Y. Zhang, W. Mu, N. Wang, W. Zhang, Z. Weng, CALPHAD-guided design of corrosion-resistant cobalt-based high-entropy alloys with strength-ductility synergy achieved through V, Nb, and Ta alloying, Intermetallics (Barking) 191 (2026) 109158, https://doi.org/10.1016/j.intermet.2026.109158.

[4] L. Shen, Y. Li, W. Zhang, S. Zhang, S. Ma, F. Peng, Z. Wu, Machine learning-assisted design of strong and ductile BCC high-entropy alloys, Mater. Res. Lett. 13 (2025) 1260–1268, https://doi.org/10.1080/21663831.2025.2577751.

[5] J. Yuan, L. Wang, C. Wang, G. Dong, J. Wang, Y. Li, J. Hu, W. Xu, Synergizing TWIP and TRIP effects for optimized mechanical performance via stacking fault energy control in austenitic steels, Arch. Civil Mech. Eng. 25 (5) (2025) 277, https://doi.org/10.1007/s43452-025-01333-0.

[6] Y.-C. Zhao, H.-W. Ma, J.-D. Sun, J.-H. Luo, Y. Su, L. Feng, T.-Z. Liu, F.-Q. Zhan, Z.-Q. Yu, T. Yang, D.-X. Liu, P.K. Liaw, Y.-C. Zhao, H.-W. Ma, J.-D. Sun, Y. Su, L. Feng, T.-Z. Liu, F.-Q. Zhan, D.-X. Liu, Z.-Q. Yu, J.-H. Luo, T. Yang, P.K. Liaw, A *Xanthium sibiricum* biomimetic Fe-based medium-entropy alloy with significant antibacterial and mechanical behaviors, Rare Metals 44 (7) (2025) 4913–4935, https://doi.org/10.1007/s12598-024-03097-7.

[7] B. Cantor, I.T.H. Chang, P. Knight, A.J.B. Vincent, Microstructural development in equiatomic multicomponent alloys, Mater. Sci. Eng. A 375–377 (2004) 213–218, https://doi.org/10.1016/J.MSEA.2003.10.257.

[8] J.W. Yeh, S.K. Chen, S.J. Lin, J.Y. Gan, T.S. Chin, T.T. Shun, C.H. Tsau, S.Y. Chang, Nanostructured *h*igh-*e*ntropy *a*lloys with *m*ultiple *p*rincipal *e*lements: *n*ovel *a*lloy *d*esign *c*oncepts and *o*utcomes, Adv. Eng. Mater. 6 (2004) 299–303, https://doi.org/10.1002/ADEM.200300567.

[9] Z. Li, C.C. Tasan, K.G. Pradeep, D. Raabe, A TRIP-assisted dual-phase high-entropy alloy: grain size and phase fraction effects on deformation behavior, Acta Mater. 131 (2017) 323–335, https://doi.org/10.1016/J.ACTAMAT.2017.03.069.

[10] S. Hun Shim, H. Pouraliakbar, S. Ig Hong, High strength dual fcc phase CoCuFeMnNi high-entropy alloy wires with dislocation wall boundaries stabilized by phase boundaries, Mater. Sci. Eng. A (2021), https://doi.org/10.1016/j.msea.2021.141875.

[11] A. Parakh, M. Vaidya, N. Kumar, R. Chetty, B.S. Murty, Effect of crystal structure and grain size on corrosion properties of AlCoCrFeNi high entropy alloy, J. Alloys Compd. 863 (2021) 158056, https://doi.org/10.1016/J.JALLCOM.2020.158056.

[12] Q. Tian, G. Zhang, K. Yin, L. Wang, W. Wang, W. Cheng, Y. Wang, J.C. Huang, High temperature deformation mechanism and microstructural evolution of relatively lightweight AlCoCrFeNi high entropy alloy, Intermetallics (Barking) 119 (2020) 106707, https://doi.org/10.1016/J.INTERMET.2020.106707.

[13] J.G. Lopes, A. Candeias, P. Agrawal, J. Shen, N. Schell, R.S. Mishra, J.P. Oliveira, Role of TiB2 inoculation particles during welding of a AlCoCrFeNi high entropy alloy, J. Alloys Compd. 995 (2024) 174694, https://doi.org/10.1016/J.JALLCOM.2024.174694.

[14] J. Shen, P. Agrawal, T.A. Rodrigues, J.G. Lopes, N. Schell, Z. Zeng, R.S. Mishra, J. P. Oliveira, Gas tungsten arc welding of as-cast AlCoCrFeNi2.1 eutectic high entropy alloy, Mater. Des. 223 (2022) 111176, https://doi.org/10.1016/J.MATDES.2022.111176.

[15] J.P. Oliveira, J. Shen, Z. Zeng, J.M. Park, Y.T. Choi, N. Schell, E. Maawad, N. Zhou, H.S. Kim, Dissimilar laser welding of a CoCrFeMnNi high entropy alloy to 316 stainless steel, Scr. Mater. 206 (2022) 114219, https://doi.org/10.1016/J.SCRIPTAMAT.2021.114219.

[16] H. Nam, S. Park, N. Park, Y. Na, H. Kim, S.J. Yoo, Y.H. Moon, N. Kang, Weldability of cast CoCrFeMnNi high-entropy alloys using various filler metals for cryogenic applications, J. Alloys Compd. 819 (2020) 153278, https://doi.org/10.1016/J.JALLCOM.2019.153278.

[17] J.P. Oliveira, A. Shamsolhodaei, J. Shen, J.G. Lopes, R.M. Gonçalves, M. de Brito Ferraz, L. Piçarra, Z. Zeng, N. Schell, N. Zhou, H. Seop Kim, Improving the ductility in laser welded joints of CoCrFeMnNi high entropy alloy to 316 stainless steel, Mater. Des. 219 (2022) 110717, https://doi.org/10.1016/J.MATDES.2022.110717.

[18] J. Shen, R. Gonçalves, Y.T. Choi, J.G. Lopes, J. Yang, N. Schell, H.S. Kim, J. P. Oliveira, Microstructure and mechanical properties of gas metal arc welded CoCrFeMnNi joints using a 308 stainless steel filler metal, Scr. Mater. 222 (2023) 115053, https://doi.org/10.1016/J.SCRIPTAMAT.2022.115053.

[19] J. Shen, R. Gonçalves, Y.T. Choi, J.G. Lopes, J. Yang, N. Schell, H.S. Kim, J. P. Oliveira, Microstructure and mechanical properties of gas metal arc welded CoCrFeMnNi joints using a 410 stainless steel filler metal, Mater. Sci. Eng. A 857 (2022) 144025, https://doi.org/10.1016/J.MSEA.2022.144025.

[20] H. Nam, S. Park, E.-J. Chun, H. Kim, Y. Na, N. Kang, Laser dissimilar weldability of cast and rolled CoCrFeMnNi high-entropy alloys for cryogenic applications, Sci. Technol. Weld. Join. (2019) 1–8, https://doi.org/10.1080/13621718.2019.1644471.

[21] N.K. Adomako, G. Shin, N. Park, K. Park, J.H. Kim, Laser dissimilar welding of CoCrFeMnNi-high entropy alloy and duplex stainless steel, J. Mater. Sci. Technol. 85 (2021) 95–105, https://doi.org/10.1016/J.JMST.2021.02.003.

[22] R. Sokkalingam, V. Muthupandi, K. Sivaprasad, K.G. Prashanth, Dissimilar welding of Al0.1CoCrFeNi high-entropy alloy and AISI304 stainless steel, J. Mater. Res. 34 (2019) 2683–2694, https://doi.org/10.1557/JMR.2019.186.

[23] J. Li, W. Wei, H. Zhang, Z. Yao, M. Chen, X. Zhao, G. Yin, X. Yang, On the investigation of microstructure and mechanical properties of the AlCoCrFeNi2.1/316 L dissimilar spot-welded joint, Mater. Today Commun. 41 (2024) 110990, https://doi.org/10.1016/J.MTCOMM.2024.110990.

[24] L. Zhu, G. Chen, X. Teng, Z. Gan, J. Zhao, C. Yang, X. Leng, Microstructure evolution and mechanical properties of electron beam welded AlCoCrFeNi2.1 eutectic high-entropy alloy/304 stainless steel joints, Intermetallics (Barking) 186 (2025) 108971, https://doi.org/10.1016/J.INTERMET.2025.108971.

[25] M. Ma, W. Wei, H. Zhang, Z. Yao, Y. Sun, M. Chen, F. Wu, Dissimilar gas tungsten arc welding of AlCoCrFeNi2.1 eutectic high entropy alloy to 316L stainless steel, J. Mater. Res. Technol. 35 (2025) 7065–7073, https://doi.org/10.1016/J.JMRT.2025.03.044.

[26] Z. Ma, W. Liu, W. Li, J. Song, H. Liu, Z. Lv, T. Wang, G. Hu, S. Peng, F. Wang, Y. Zhao, H. Zhang, Microstructure evolution, composition distribution, and crack formation mechanisms of SS 316L/IN718 graded materials fabricated by laser directed energy deposition, J. Mater. Process. Technol. 340 (2025) 118843, https://doi.org/10.1016/J.JMATPROTEC.2025.118843.

[27] S. Kou, Welding metallurgy, Welding Metallurgy (2002), https://doi.org/10.1002/0471434027.

[28] J.G. Lopes, J.P. Oliveira, A short review on welding and joining of high entropy alloys, Metals (Basel) 10 (2020) 212, https://doi.org/10.3390/met10020212.

[29] X. Li, Y. Zhao, Y. Peng, S. Shi, K. Liu, G. Xu, Y. Lei, N. Lu, H. Wang, X. Lin, Bulk single-crystal-like IN738 alloy fabricated using laser powder bed fusion by controlling the thermal flow, Mater. Res. Lett. 13 (2025) 1072–1079, https://doi.org/10.1080/21663831.2025.2563357.

[30] W. Kurz, D. Fisher, Fundamentals of Solidification, 1998.

[31] J.G. Lopes, P. Rocha, D.A. Santana, J. Shen, E. Maawad, N. Schell, F.G. Coury, J. P. Oliveira, Impact of *a*rc-*b*ased *w*elding on the *m*icrostructure *e*volution and *m*echanical *p*roperties in *n*ewly *d*eveloped Cr29.7Co29.7Ni35.4Al4Ti1.2 *m*ulti-*p*rincipal *e*lement *a*lloy, Adv. Eng. Mater. 25 (2023) 2300109, https://doi.org/10.1002/ADEM.202300109.

[32] D. Choudhuri, S. Shukla, P.A. Jannotti, S. Muskeri, S. Mukherjee, J.T. Lloyd, R. S. Mishra, Characterization of as-cast microstructural heterogeneities and damage mechanisms in eutectic AlCoCrFeNi2.1 high entropy alloy, Mater. Charact. 158 (2019) 109955, https://doi.org/10.1016/J.MATCHAR.2019.109955.

[33] T. Xiong, S. Zheng, J. Pang, X. Ma, High-strength and high-ductility AlCoCrFeNi2.1 eutectic high-entropy alloy achieved via precipitation strengthening in a heterogeneous structure, Scr. Mater. 186 (2020) 336–340, https://doi.org/10.1016/J.SCRIPTAMAT.2020.04.035.